Chemical Engineering Journal 475 (2023) 146064

Contents lists available at ScienceDirect

Chemical Engineering Journal

journal homepage: www.elsevier.com/locate/cej

Fast deployable real-time bioelectric dissolved oxygen sensor based on a multi-source data fusion approach

Yongyun Li [a], Yahui Chen [a], Yi Chen [b], Renwei Qing [a], Xinyu Cao [a], Peng Chen [a], Wei Liu [c], Yao Wang [c], Guangwu Zhou [d], Heng Xu [a], Likai Hao [e,f,g], Can Wang [h], Shun Li [i,j], Yongguan Zhu [f,i,j], Stefan Haderlein [k], Fei Xu [a,*]

[a] Key Laboratory of Bio-Resource and Eco-Environment of Ministry of Education, College of Life Sciences, Sichuan University, Chengdu 610065, Sichuan, PR China
[b] Sichuan Aerospace Fenghuo Servo Control Technology Corporation, Chengdu 611130, Sichuan, PR China
[c] Institute of New Energy and Low-Carbon Technology, Sichuan University, Chengdu 610065, Sichuan, PR China
[d] School of Aeronautics and Astronautics, Sichuan University, Chengdu 610065, Sichuan, PR China
[e] State Key Laboratory of Environmental Geochemistry, Institute of Geochemistry, CAS, Guiyang 550081, PR China
[f] University of Chinese Academy of Sciences, Beijing 100049 PR China
[g] CAS Center for Excellence in Quaternary Science and Global Change, Xi'an 710061, PR China
[h] School of Life Science and Engineering, Southwest Jiaotong University, Chengdu 610031, Sichuan, PR China
[i] Key Laboratory of Urban Environment and Health, Ningbo Observation and Research Station, Institute of Urban Environment, CAS, Xiamen 361021 PR China
[j] Zhejiang Key Laboratory of Urban Environmental Processes and Pollution Control, CAS, Haixi Industrial Technology Innovation Center of Beilun, Ningbo 315830, PR China
[k] Environmental Mineralogy and Chemsitry, Department of Geosciences, University of Tuebingen, Tuebingen 72076, Germany

ARTICLE INFO

Keywords:
Dissolved oxygen
Biosensor
Integrated microbial fuel cell
GA-BPNN
Multi-source data fusion

ABSTRACT

Commercially available dissolved oxygen (DO) sensors are hardly suitable for stereoscopic and precise DO monitoring due to their design, high cost and susceptibility to matrix effects. Here, we have developed a DO biosensor based on an integrated chamber-free microbial fuel cell (DO_{MFC}) as the core and a Raspberry Pi microcomputer as the data acquisition system. This biosensor is low cost, readily available and compact in configuration. To this end, stable microbial biofilms with oxygen gradients were established on bioaffinity aluminum foam as anode. The DO_{MFC} sensor has a low internal resistance (9.62 Ω) that can respond to DO changes in less than one minute and produce a reliable voltage signal to record DO (0.15–9.5 mg/L) under challenging conditions. After training the GA-BPNN model with multidimensional data by automatically applying a data fusion strategy from multiple sources, accurate DO predictions (R^2 = 0.997, *RMSE* = 0.0447, *MAE* = 0.0401) were obtained. The DO_{MFC} sensor and the prediction model showed excellent agreement (R^2 = 0.954) in complex natural applications (different pH values, conductivities, water temperatures, etc.), covering a wide range of applications. Since the sensor mini-monitoring system is inexpensive and easy to make and use on a large scale, it is a promising alternative for oxygen measurements in both natural and artificial waters.

1. Introduction

Dissolved oxygen (DO) is a key environmental parameter in determing the quality of natural and artificial waters. Eutrophication and climate extremes can cause a dramatic reduction of DO in natural waters, adversely impacting on biological metabolisms and water self-purification processes and causing irreversible damages to aquatic ecosystems [1]. Reducing carbon footprint and attaining carbon neutrality can mitigate the potential for climate crises, while power-saving is a critical pathway to achieve this strategic purpose [2]. The wastewater treatment facilities often apply extensive constant aeration to maintain the DO level, ensure high aerobic microbial metabolism activities and guarantee the effluent quality. The aeration generally consumes >50% of the electricity demand, and the inability to achieve on-demand aeration is the main cause of such high electricity consumption [3,4]. A precise control of the aeration system will contribute significantly to save energy and reduce carbon emissions. Thus, a deployable, low-cost sensor system, which can acquire multi-depth DO

* Corresponding author.
E-mail address: xufei@scu.edu.cn (F. Xu).

https://doi.org/10.1016/j.cej.2023.146064
Received 27 June 2023; Received in revised form 15 August 2023; Accepted 13 September 2023
Available online 16 September 2023

data in real-time, would be applicable for both fast water quality analysis and optimization of waste water treatment.

Commercialy available DO sensors are mainly based on electrochemical or fluorescence quenching principles and techniques. The monitoring of DO by an electrochemical sensor relied on the electrode's redox-generated current. However, electrolytes and membranes are prone to foul under harsh operating conditions and thus require frequent routine replacement. In contrast, the fluorescence quenching-based DO sensor has the advantages of being electrolyte-free and highly accurate. Nevertheless, it is often expensive and unsuitable for larger-scale implementation. Addtionally, the sensor tip is fragile and sensitive to damage by scratchthese, loss of the built-in fluorescent substance and air bubbles may seriously affect detection effciency [5]. Therefore, developing an affordable accurate and resilient *in situ* real-time DO monitoring system is waranted for broad range of applications in science and technique developments.

Microbial fuel cell (MFC) technology is a poorly expored but promising alternative technology for DO monitoring. The electrons obtained from the catalytic degradation of organics by electrochemically active bacteria (EAB) at the anode are combined with the cathode electron acceptor via an external circuitwith molecular oxygen as electron acceptor [6,7] (Eq. (1)).

$$O_2 + 4H^+ + 4\ e^- \rightarrow 2\ H_2O\ (E_0 = +1.229\ V\ \text{measured versus SHE}) \quad (1)$$

With cathodic oxygen reduction (ORR) as the rate-limiting step, the MFC's electrical signal (voltage and/or current) output would reflect the dynamic DO variation in real time. The feasibility of single-chamber MFCs to monitor DO has been shown recently [8–10]. However, conventional MFCs require the assembly of bulky anaerobic anode chambers and frequent replenishment of sediments or other materials to "fuel" the EABs, thus limiting their wide application [11–13]. Regarding data evaluation, also some shortcomings of predictive models and algorithms need to be overcome: (1) Due to the combined influence of unknown biological activities and environmental parameters (pH, water temperature, etc.), the DO change is often highly non-linear and the calibration obtained by a single-factor experiment is not robust. (2) Linear and polynomial models often fail to handle data that is non-linear or correlated [14]. (3) Manual data collection results in a relatively limited small training dataset, creating problems for model training and MFC sensor calibration. These flaws prevent MFC biosensors from achieving real-time monitoring and affect long-term stability.

Here, we designed and successfully applied a bioelectric DO sensor using an integrated chamber-free microbial fuel cell, which is compact, does not require anolyte replenishment, and is truly plug-and-play [15]. This DO_{MFC} operates sensitively and outputs reliable signals under complex natural conditions and can is suited to overcome the above-mentioned technical difficulties at moderate costs. The novel operation mechanism was investgated in-depth using electrochemistry, microscopy, and microbiological techniques. Raspberry Pi was applied as a host to collect and transmit the data to the Internet of Things (IoT) platform [16]. Multiple water-quality parameters were considered to construct the genetic algorithm optimized back propagation neural network (GA-BPNN) for auto-compensation of systematic drift caused by changes in operating conditions.

This novel approach demonstrates the robustness and practicability of combining bioelectrochemical and multi-source data fusion techniques for accurate monitoring of dissolved oxygen, and is expected to build an exemplary and field-deployable DO monitoring system and network platform.

2. Materials and methods

2.1. Experimental system setup

2.1.1. DO_{MFC} setup

The DO_{MFC} was redesigned and improved from the previously reported iMFC [15], using an aluminum (Al) foam plate loaded with the domesticated sludge as the anode and carbon cloth modified with a platinum-based and metal–organic framework (MOF)-derived Fe-N-C catalysts as the cathode (Fig. S1-2). A bacterial cellulose membrane (BCM) separated the anode and cathode to avoid short circuit. Two identical titanium meshes were set up as the current collector (Fig. 1B).

Before assembly, the anodes were incubated in serum bottles containing municipal anaerobic sludge for 3 days. Polarisation and power density curves were recorded at different external resistances (50 Ω to 10 KΩ), each held for 30 min. The influence of different anode/cathode area ratios (4:3 versus 2:1) on the sensor performance was also explored by varying the cathode area of DO_{MFC} in batch mode. A MFC-based DO sensor setting in a cylindrical configuration was used as a control, whose structure and operational results were presented in the Supplementary Material. Unless otherwise stated, the culture medium contained acetate and trace elements as listed in the Supplementary Material (Kuntke et al. 2012). All reagents were suppplied by Aladdin Biochemical Technology Co., Ltd, (Shanghai, China).

2.1.2. Data acquisition platform setup

RPI.GPIO library provides a Python module to control the general-purpose input/output (GPIO) on Raspberry Pi. The Raspberry Pi's GPIO/BCM pin 7 captures data from the water temperature sensor (DS18B20, DFRobot Co., Ltd., Shanghai, China) through the 1-Wire protocol according the mannuals. ADS1263 chip module (Waveshare Electronics, Shenzhen, China) was used to amplify DO_{MFC} output voltage and conductivity signal for final signal processing. Analog voltage values were converted into digital signals and then collected by Raspberry Pi 4B (ARMv7 architecture). The DO_{MFC} was connected to ADS1263 chip module pins via an alligator clip to the female jumper wire. A dual-channel isolated RS485 expansion board (Waveshare Electronics Co., Ltd., Shenzhen, China) adds an RS485 interface for Raspberry Pi. RS485 communication protocol enables the Raspberry Pi to acquire the data collected by the pH meter or detector (Rirans Electronics Co., Ltd., Shenzhen, China) and fluorometric DO probe (Jingxun Changtong Electronic Technology Co., Ltd., Weihai, Shandong, China). The role of the DO electrode is to assess the accuracy of the prediction model. Raspberry Pi works as the IoT gateway end through the TCP/IP protocol connected to China Mobile's OneNET cloud platform to achieve water-quality data collection and online wirless transmission. PC accesses cloud dataset to build, validate, and optimize neural network models (Fig. 1A).

A polymethyl methacrylate reactor (20 × 10 × 10 cm) was employed to investigate the DO_{MFC} performance in the lab (Fig. 1B-C). A peristaltic pump was used to provide controllable hydraulic retention time (HRT). A magnetic stirrer was applied to reduce the concentration polarization at the electrode-solution interface.

2.2. DO_{MFC} performance evaluation

2.2.1. Anode domestication

Adaptive domestication of anodic microbial biofilm communities was performed under oxygen-rich conditions at 25 °C. The DO_{MFC} was immersed in a 500-mL beaker (400 mL acetate medium). Aeration was applied at a flow rate of 0.5 L/min to keep the DO at a saturation level. Operating conditions were optimized by evaluating the output voltage level and stability of DO_{MFC} loads with different external resistances (1 kΩ, 2 kΩ, 4.7 kΩ and 5.7 kΩ).

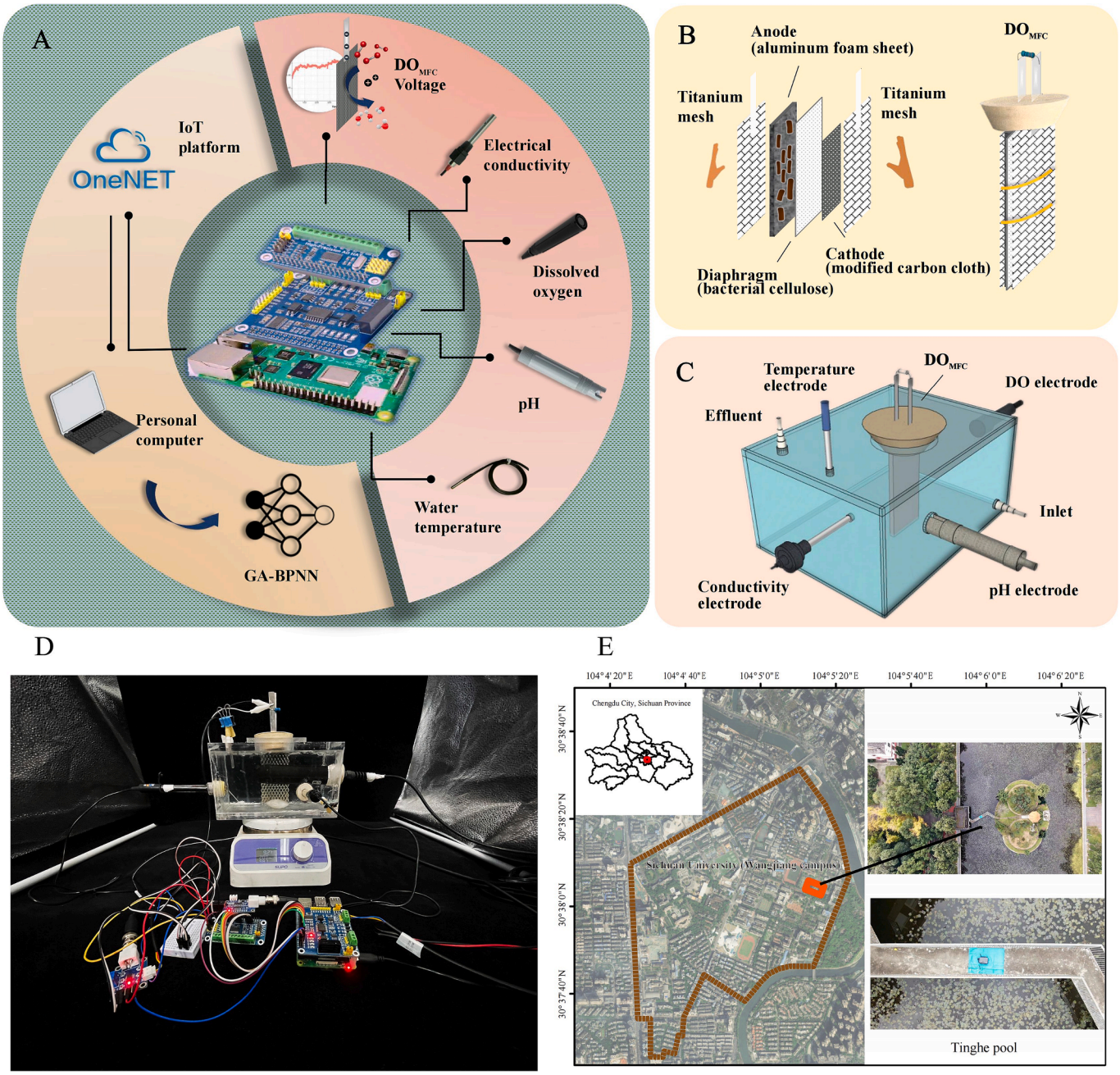

Fig. 1. The DOMFC and data fusion system. (A) Data acquisition and analysis system. (B) Schematic diagram of DOMFC assembly process. (C) Upflow reactor for lab-scale experiments. (D) The practical operation of DOMFC in the laboratory. (E) Field tests using DOMFC.

2.2.2. *Dynamic response characteristics*

Synchronous dynamic monitoring of the voltage and water quality data was conducted in batch mode at room temperature (Fig. 1D). During an entire batch mode operating cycle, the reactor was filled with acetate medium, and refilled until the DO stopped decreasing. The Raspberry Pi-based data acquisition system automatically collected the data read by each water quality probe. The data were collected to evaluate the operational performance characteristics of DO_{MFC} and build machine learning models.

The fluid inside the reactor was circulated in a continuous mode at room temperature with the influent (the same acetate medium in a feed tank) to examine the signal response of the sensor to different DO (Fig. S3). The influent from the feed tank was continuously pumped into the reactor using a peristaltic pump. Influent with different DO was prepared by purging N_2 or O_2. The sensitivity and response time of DO_{MFC} were investigated by intermittent aeration (single aeration time was 10 min) at different hydraulic retention times (HRTs), with the aeration interval depending on the microbial DO consumption. To further validate the applicability of DO_{MFC}, the voltage response to DO was verified using glucose containing artificial wastewater, artificial polluted river water and artificial juice wastewater instead of acetate medium, respectively. Artificial wastewater formulations are available in the Supplementary material.

2.2.3. *Machine learning modeling and model optimization*

The dynamic monitoring data were plotted to establish the linear relationship between DO and the independent variables by ordinary least squares (OLS) regression. A predictive model based on a genetic algorithm optimized back propagation neural network (GA-BPNN) was constructed using MATLAB (version R2016b, The Math Works®, Natick,

MA, USA). Back-propagation neural network (BP-NN) was beneficial for multicollinear explanatory variables in regression analysis due to its generalization, approximation, and adaptive learning capabilities. Herein, the genetic algorithm (GA) is employed to optimize the initial weights and thresholds of the BP-NN (Sun and Xu 2016). The topology of the BPNN was determined first, followed by the initialization of the model weights and thresholds. The DO concentration was used as the control factor, while other indicators were used as response characteristics. The dataset was divided into training and test sets. The validation set was created by splitting the training set by the "newff" function (which creates a feed-forward back-propagation network) while the model was being trained. The training error was used as the input of the fitness function (Formula (1)), and the optimal fitness value was obtained by iteratively optimizing the hyperparameters until convergence through the selection, crossover, and mutation strategies of the GA [17]. After screening the individuals with the best fitness value, the initial weights and thresholds of the BP neural network were optimized accordingly. GA-BPNN was trained using the dataset, and convergence speed and prediction accuracy significantly improved (Fig. S4A). The detail structure flow chart of GA-BPNN is shown in Fig. S4B.

$$F = k(\sum_{i=1}^{n} |y_i - o_i|) \quad (1)$$

where y_i and o_i represent the expected output and predicted output of the i-th node, respectively, and k is the coefficient.

2.2.4. In-situ DO sensing performance

In situ field experiments were conducted in the Tinghe Pool (30°38′16 N, 104°5′47.04″ E), Sichuan University, Chengdu, Sichuan Province (Fig. 1E), where water lilies were planted. The water depth in this area is about 45 cm, and precipitation is the primary water input. The basic physicochemical properties of the water were described in Table S1-2. The DO_{MFC} and data acquisition system operated continuously for 20 days at 5 mins per round.

2.3. Electrochemical analysis

The electrochemical behaviors of the DO_{MFC} electrodes were determined using CHI 760E electrochemical workstation (Chenhua Instrument Co., Ltd., Shanghai, China), equipped with a standard three-electrode system. The system consists of a working electrode (anode or cathode), a counter electrode (Pt sheet), and a reference electrode (Ag/AgCl electrode). The electrochemical behavior of DO_{MFC} was also investigated by cyclic voltammetry (CV) and linear sweep voltammetry (LSV). Anode and cathode CV tests were performed between −1 to 1 V and −0.25 to 1.0 V, respectively, at a scan rate of 50 mV/s. Cathode LSV tests were conducted at potentials from −0.15 to 0.85 V with a scan rate of 10 mV s^{-1}. The internal impedance of DO_{MFC} was calculated using electrochemical impedance spectroscopy (EIS) analysis. The EIS analysis was conducted in the frequency range 0.1 Hz-100 kHz with an alternating current (AC) perturbation of 5 mV. Prior to the test, the MFC-based sensor operated in an open circuit until the voltage stabilized.

2.4. Illumina MiSeq sequencing and microbial community analysis

The microscopic effect of dynamic oxygen change on the DO_{MFC} was studied by analyzing the anodic microbial biofilm community structure and diversity. After adaptive domestication, the DO_{MFC}s continued work for 2 weeks in aeration (oxygen saturation), batch and anoxic (DO < 2 mg/L) modes for preparing different anode samples. In addition, the sludge sample was used as the control for high-throughput sequencing to investigate the evolution of the active microbial community after domestication. Total RNA was extracted using the TIANamp Bacteria RNA Kit (Tiangen Biotech Co., Ltd, Beijing, China) according to the manufacturer's instructions. The quantity and quality of the extracted RNA were assessed using a NanoDrop NC2000 spectrophotometer (Thermo Fisher Scientific Inc., Waltham, MA, USA) and agarose gel electrophoresis. Reverse transcription of RNA was performed using PrimeScrip™ One-Step RT-PCR Kit Ver. 2 (TaKaRa Biotechnology Co., Ltd., Dalian, China) [18]. The V3-V4 hypervariable regions of the 16S rRNA gene were amplified with primers 338F (5′-ACTCCTACGGGAGGCAGCAG-3′) and 806R (5′-GGACTACHVGGGTWTCTAAT-3′). Amplified products were purified by Hieff NGS DNA Selection Beads (Yeasen Biotechnology Co., Ltd., Shanghai, China). Subsequently, the purified amplicons were sequenced on an Illumina Novaseq PE250 platform (Illumina, San Diego, CA, USA) at Shanghai Personal Biotechnology Co., Ltd. (Shanghai, China). PCR reaction conditions and sequencing data analysis are available in the Supplementary Material.

2.5. Characterization of electrodes

The three-dimensional morphology of anodic microbial biofilms was imaged under confocal laser scanning microscope (CLSM, LSM880 Zeiss, Germany), and the activity of biofilm was evaluated by viability staining with SYTO 9 and propidium iodide (PI) (Thermo-Fisher Scientific, Pittsburgh, PA, USA). A microelectrode system (EasySensor Ltd., Nanjing, China) was used to analyze the profile distribution of DO from the biofilm surface to the Al foam pores. A motor controlled the movement of the DO microelectrode stepwise.

Morphological characteristics of DO_{MFC} electrodes and diaphragm before and after operation were analyzed by a field emission-scanning electron microscope (FE-SEM, SU8010, Hitachi, Japan) equipped with energy dispersive spectroscopy (EDS) for elemental analysis. Samples were air dried.

2.6. Analyses and calculations

The accuracy of the model was evaluated by the root mean square error (*RMSE*), mean absolute error (*MAE*) and R-squared (R^2). Residual analysis was used to judge the fitting effect of the regression model. The calculation formulas of the above analysing methods are shown in the Supplementary Material. Data processing and visualization were conducted using the R (Version 4.1.3, https://www.r-project.org) and Origin Pro8 software (Originlab, Northampton, MA, USA).

3. Result and discussion

3.1. DO_{MFC} operational performance

Fig. 2A shows that after 30 mins of stabilization, the open-circuit voltage of the DO_{MFC} was as high as 0.867 V. When the value of external resistance was in the range of 2–10 kΩ, there was a sharp voltage drop as the oxidation/reduction reaction started to consume energy [19]. The DO_{MFC} voltage reached 0.702 V at an external load of 10 kΩ external resistance, yet the power density was only 41.067 mW/m^2. In comparison, the DO_{MFC} obtained a maximum power density of 157.69 mW/m^2 at 1 kΩ with a voltage of 0.435 V. Although the DO_{MFC} also achieved a high power output at 500 Ω (147.02 mW/m^2), a further voltage drop will significantly affect the sensitivity to DO monitoring [12]. In addition, the high current due to the low resistance will increase oxygen consumption, thus affecting the monitoring environment [11]. With simultaneous consideration of the importance of power density for components such as electrodes and microorganisms and the necessity of high voltages for accurate DO monitoring, the resistors of 1 kΩ, 2 kΩ, 4.7 kΩ and 5.7 kΩ were selected for the next study [20].

During anode domestication, the voltage may be difficult to increase with cultivation time due to oxygen stress. The DO_{MFC} quickly achieved high-voltage output at external loads of 1 kΩ, 2 kΩ, and 4.7 kΩ with maximum voltages of 0.428 V, 0.491 V, and 0.636 V, respectively (Fig. 2B). The voltage of the DO_{MFC} with a 4.7 kΩ external resistor gradually decreased and finally stabilized at 0.606 V. The DO_{MFC} voltage

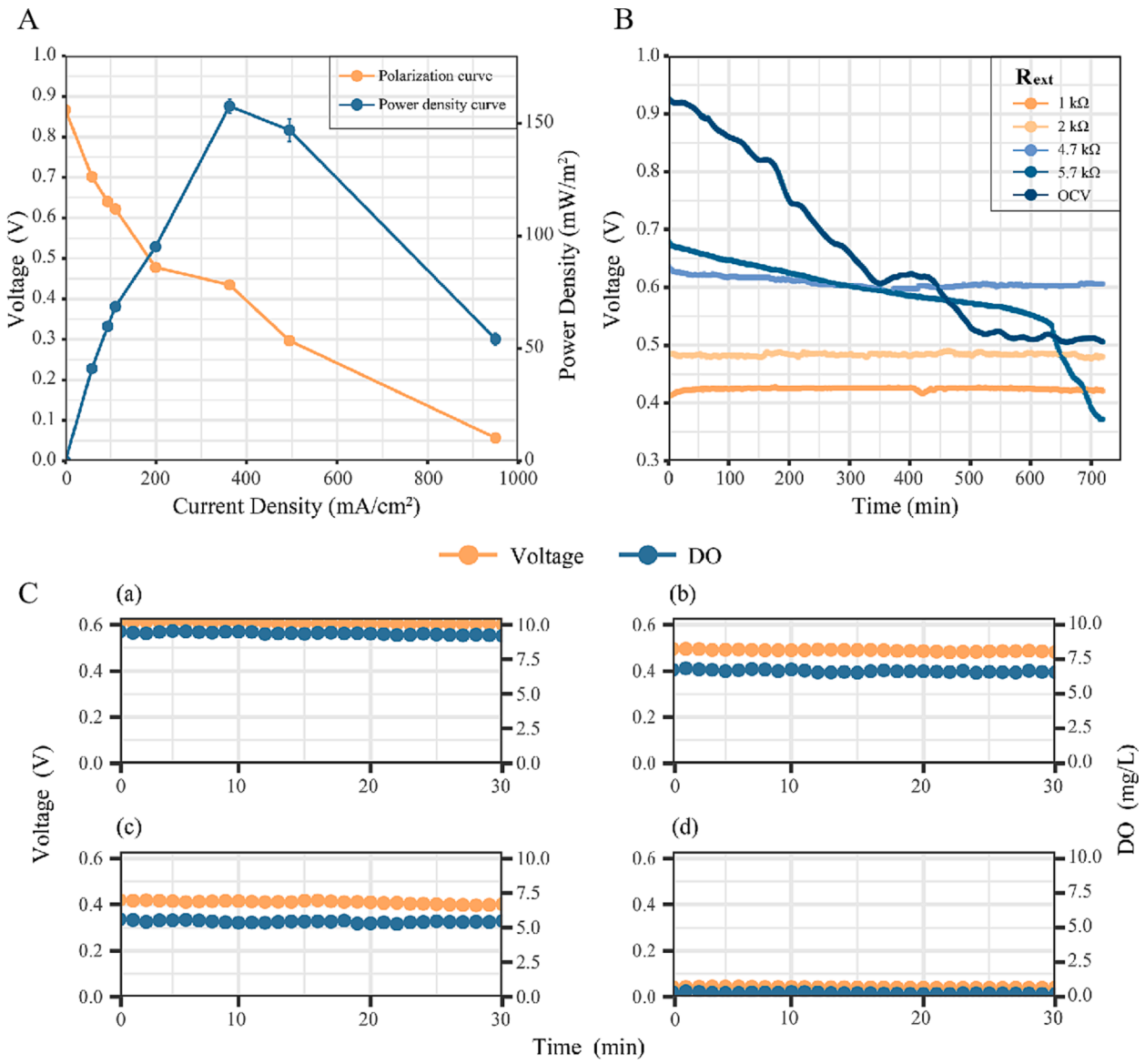

Fig. 2. The electrical performance of DOMFC. (A) Polarization curve and power density curve obtained from the DOMFC. (B) Voltage output of DOMFC under oxygen-replete conditions. (C) Stability of DOMFC for sustained response to different levels of dissolved oxygen.

with a 5.7 kΩ external resistor dropped irreversibly and continuously relative to other external resistance values. Thus, the external resistance of 4.7 kΩ was used for all subsequent studies to maximize voltage output. A relatively high resistance favors the enrichment of electroactive bacteria (EAB) over methanogens [21]. However, a rapid voltage collapse was observed when operating under open-circuit conditions or with an external resistance of 5.7 kΩ. A plausible explanation is that when there is little or no current, the metabolism and activity of EABs will be affected [22,23]. Another reasonable speculation is that electron transfer is thermodynamically unfavorable when the anode potential is too negative, thus the cells cannot capture energy efficiently.

The DO_{MFC} maintained a stable voltage output (different voltage levels, 0.607 ± 0.003, 0.489 ± 0.004, 0.410 ± 0.07, and 0.041 ± 0.002 V, respectively) for 30 mins at a fixed DO (different DO gradients, 9.39 ± 0.10, 6.66 ± 0.11, 5.43 ± 0.08, and 0.27 ± 0.05 mg/L, respectively) (Fig. 2C). Also, the anode potential was relatively constant (-0.472 ± 0.013 V versus Ag/AgCl), and there is no significant difference under different DO gradients (Table S3). The coefficient of variation (CV) of voltage gradually increased with decreasing gradient of DO, which were 0.544%, 0.838%, 1.608% and 4.978%, respectively. This may be related to the fact that the mass transfer process of DO at the cathodic interface was affected at low concentrations [24]. However, the continuous and relatively smooth output signal is still indirect evidence of the DO_{MFC}'s reliability and specific responsiveness of the cathode to DO change.

CLSM measurements showed that the biofilm attached to the anode surface was 12 to 16 μm thick. The lack of apparent stratification of live or dead bacteria (Fig. 3A) indicated that the biofilm maintained a high viability. The DO profile also indirectly reflected the growth and characteristics of the biofilm. DO concentration decreased significantly with depth, from 4.68 mg/L at the biofilm surface (0 μm) to 1.01 mg/L at 100 μm (Fig. 3B). The DO profile was across the depth profile was non linear. Between 0 and 20 μm (basically at the anode surface), the diffusive DO flux ($J_{O_2,m}$) in the biofilm was 7.7 g $O_2 \cdot m^{-2} \cdot day^{-1}$ and dropped with depth (20–100 μm, below the plane of the Al foam) to 2.239 g $O_2 \cdot m^{-2} \cdot day^{-1}$. Oxygen accelerates the inhomogeneous growth of the biofilm, enhancing biofilm complexity and porosity, allowing nutrient transport to the inner biofilm [25]. The diffusive DO flux decreased continuously during penetration due to increased mass transfer resistance and consumption by aerobes, which suggests the presence of aerobic and anoxic zones in the biofilm profile.

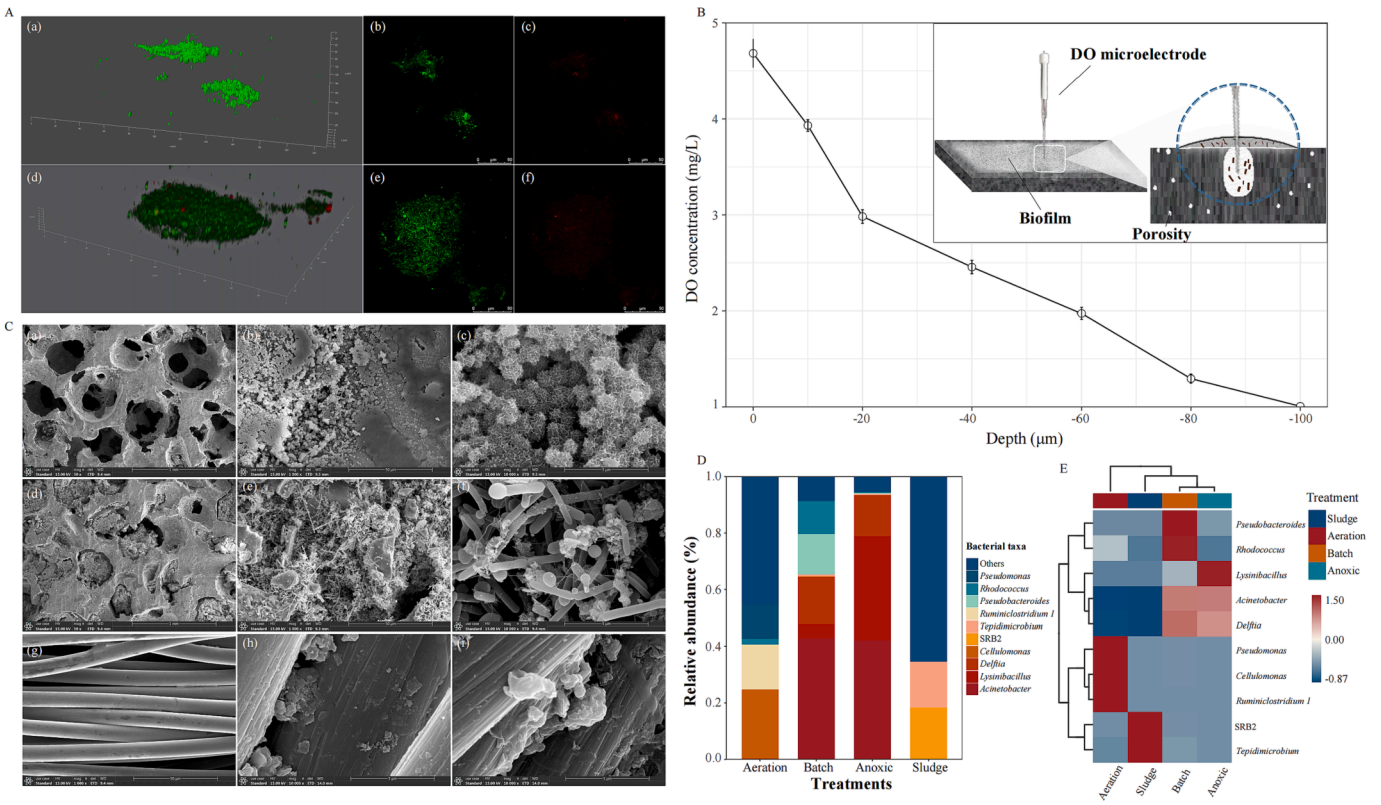

Fig. 3. Characterization of electrode morphology and analysis of anode microbial community structure. (A) CLSM images of anode biofilm after 6 (a-c) and 12 (d-f) h of operation. (B) The DO distributions inside the biofilm. (C) SEM images of the anode and cathode before and after operation. a-c: Morphological characterization of the Al foam before operation at different magnifications. d-f: Morphological characterization of the Al foam after operation at different magnifications. g: Morphological characterization of carbon cloth without catalyst loadings. h-i: Morphological characterization of carbon cloth with catalyst loadings before and after operation. (D) Analysis of anode microbial community structure at the genus level. (E) Clustered heatmap analysis based on the top 10 genera.

Traditionally, the MFC anode requires anoxic conditions as the EAB are mainly anaerobes, which reduces the applicability of MFCs [26,27]. However, the anode presented here can be populated by facultative EABs that produce electricity in suboxic or oxic environments. Small amounts of oxygen positively affect aerobic or facultative EABs' growth and extracellular electron transfer (EET), such as *Shewanella* and *Pseudomonas* [28,29]. The high voltage output of the DO_{MFC} can further be rationalized by increased biofilm thickness protects the EAB, while the inner side of the biofilm achieves stable electricity production [30]. The above findings and interpretations support the configuration design of DO_{MFC} and anode domestication procedure.

3.2. Morphology of the electrode surfaces after continuous operation

As shown in Fig. 3C a-c, the pores of the Al foam anode varied in size and roughness providing a high specific surface area, which facilitates EAB's adhesion and aggregation [31]. The internal pores of the Al foam were occupied by various bacilli and cocci, while the surface framework appeared structurally intact and smooth (Fig. 3C d-f). As an excellent signal conductor and shelter for EAB, Al foam can function as anode also under harsh conditions for long periods. Even after a long run of 20,160 mins, no noticeable structure change was found on the Al foam. In contrast, at the cathode some adhesions resembling extracellular polymers were present after extended operation, but only few individual cells were observed (Fig. 3C h-i). The smooth surface of the positively charged carbon cloth fibers apparently were difficult for the bacteria to adhere [32]. The cathode catalytic layer include non-Pt and Pt-based catalysts (Fig. S1, 5). The former uses ZIF-8 as the precursor, mixed with metal salts and pore-forming agents, followed by calcination at high temperature, providing low toxicity and long-term stability [33]. The latter relies on the domain-limiting effect of mesoporous carbon. The probability of small organic molecules contacting and poisoning the catalytically active surface of the Pt-Co alloy catalyst is reduced. In contrast, the space inside the carbon layer is sufficient for oxygen molecules to pass, thus ensuring a high ORR activity [34]. Notably, salt precipitation (mainly calcium salt) and the loss of catalyst components may inhibit the ORR activity, which impedes the long-term high-precision application. Such limiting factors should be considered and included in the subsequent research and applications.

3.3. Microbial succession

Fig. 3D-E illustrates the microbial community structure and diversity at the genus level of sludge, aeration, batch and anoxic samples. The sludge was mainly dominated by thermophilic anaerobic bacteria *Tepidimicrobium* (16.05%) and SRB2 (18.50%). After anode domestication, the microbial community structure changed dramatically. *Cellulomonas* (24.42%), *Ruminiclostridium 1* (15.89%) and *Pseudomonas* (11.82%) became dominant after aeration. *Delftia* (16.78% and 14.49%), *Lysinibacillus* (4.92% and 36.86%) and *Acinetobacter* (42.79% and 42.12%) dominated in both batch and anoxic operation mode. Two striking observations emerged from the data comparison: (1) The microbial community richness and diversity of the batch and anoxic samples were lower than that of the sludge and aerated samples (Fig. S10). (2) The sum of the relative abundance of the top 10 bacterial genera in the batch (91.46%) and anoxic (94.42%) samples was greater than that of the sludge (34.6%) and aeration (54.61%) samples.

In sludge, *Tepidimicrobium* can decompose polysaccharides such as lignin. The taxa of SRB2 are typical EAB associated with sulfate reduction, which might be responsible for the anode corrosion as presented in

Fig. S6B [35,36]. *Cellulomonas*, which dominated the aerated samples, is known for its cellulose-degradation ability [37]. Some members of *Cellulomonas* (e.g., *C. fimi*) can use cytochrome *c* (Cyt *c*) for direct EET [38]. *Lysinibacillus* can grow up to 1 mm in length and establish centimeter-scale long-distance electron transfer (LDET) networks through intercellular entanglement [39]. In the current work, the relative abundance of *Lysinibacillus* reached 36.86% and 4.92% in the anoxic and batch-operated samples, respectively. In addition, the CLSM (Fig. 3A e) and SEM (Fig. 3C e) results also demonstrated that the biofilm gradually transformed from an initial patchy distribution pattern to a dense network of long filamentous microorganisms generated by cross-linking. This phenomenon was critical for maintaining the excellent signal generation of the DO_{MFC}.

DO change drives the shift of the dominant species. The presence of oxygen usually reduced SRBs abundance, thereby reducing the risk of electrode corrosion [40]. Aerobes and facultative anaerobes accelerated substrate decomposition and achieved rapid proliferation during oxygen exposure. A microbial survival strategy that allows metabolism under hypoxic or anaerobic conditions gives facultative anaerobes a competitive advantage and may significantly contribute to electronic power production [41]. The environments of batch and anoxic samples closely resembled the sensor's actual working conditions, proving the robustness of DO_{MFC}. Typical electrogenic bacteria such as *Geobacillus* were not observed because they are strictly anaerobes, and therefore non-anaerobic species-dominated biofilms are more suitable for DO sensor development.

3.4. Electrochemical analysis

As shown in Fig. 4A, the anode CV curve was relatively symmetrical, indicating a invertible redox process was occurred due to the biofilm [42]. However, since the anode was loaded with a diverse bacterial community, specific peak assignments can be challenging [43]. Fig. 4B-C shows the electrochemical response of catalysts-modified and catalysts-free cathodes toward ORR in N_2 and O_2 saturated solutions. In the O_2 saturated solution, the CV curve of the catalysts-modified carbon cloth shifted significantly toward the negative potential, where the reduction current was caused by oxygen reduction. The current density of the catalyst-modified cathode was 3 $mA{\cdot}cm^{-2}$ at 0.25 V, while the catalyst-free cathode had no output current. Under the same condition, the CV curve area of the catalyst-modified cathode was significantly larger than the catalyst-free one. The ORR onset potential was substantially closer to the thermodynamic potential when the carbon cloth was loaded with catalysts, exhibiting its high intrinsic activity. The significant change in the CV curve area indicates that the catalyst layer significantly increased the electrochemical three-phase interface [44]. The LSV curve of the catalyst-modified cathode exhibited greater onset potential (0.605 V) than the catalyst-free cathode (0.099 V). In addition, the reduction current of the catalyst-modified cathode was higher at all potentials. The above results reveal that the catalyst-modified cathode is a signal transduction component with excellent performance under various harsh conditions.

According to the equivalent circuit diagram (Fig. 4D), the internal

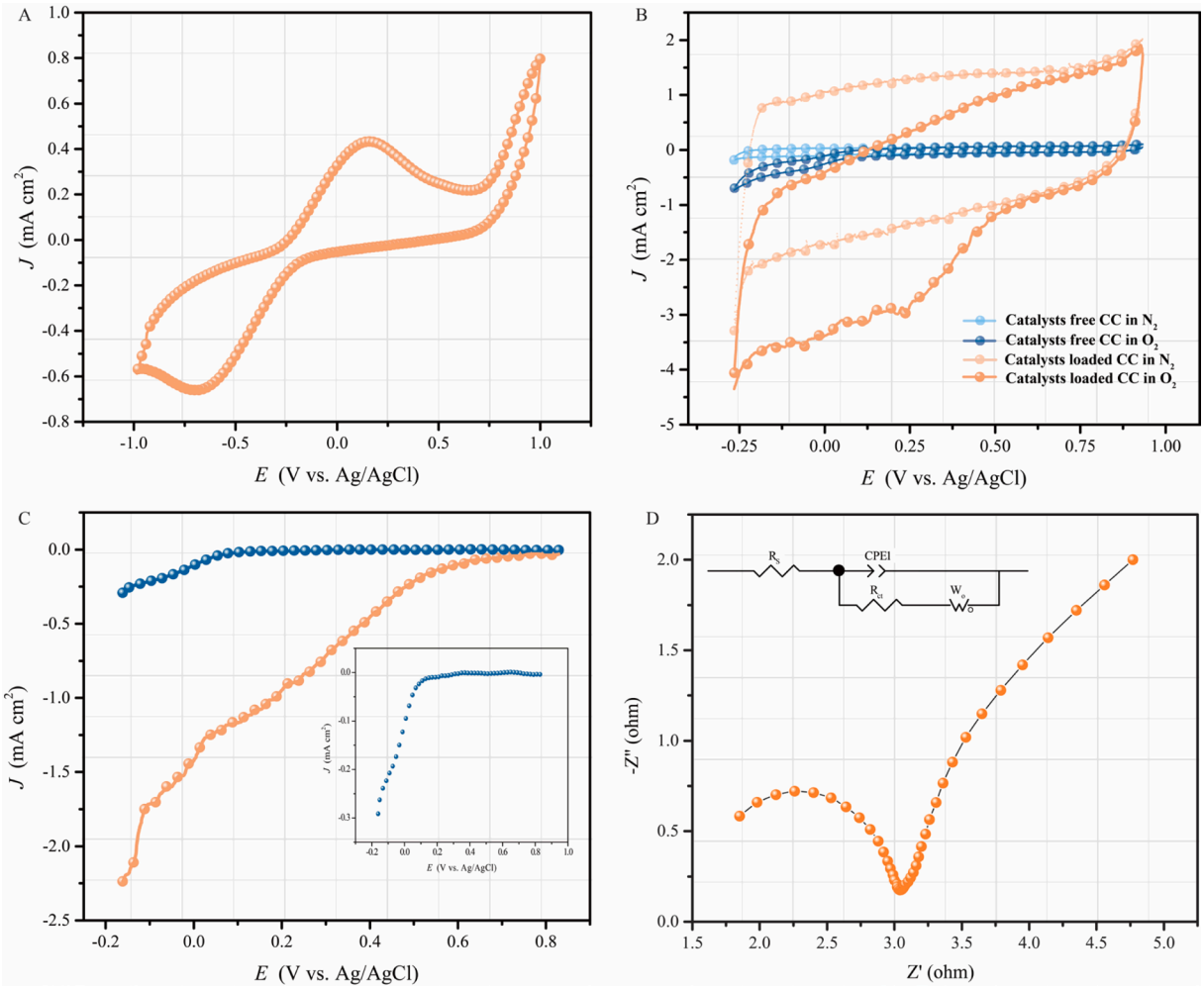

Fig. 4. Electrical performance analysis of the DOMFC. (A) CV curves of Al foam anode. (B) CV and (C) LSV curves of carbon cloth with and without catalyst loadings. (D) Nyquist plots of EIS spectra (the equivalent circuit was fitted with Zview impedance software).

resistance of DO_{MFC} was calculated to be only 9.62 Ω (Table S4), indicating high conductivity between the anode and the biofilm. The Warburg impedance was shown as a diagonal line with a slope of 45 in the low-frequency region, which correlates with electron or substrate migration at the anode surface [45]. The resistance value of Warburg impedance (W_o-R) was 6.663 Ω, indicating that the ion diffusion process contributes a significant part of the internal resistance.

A closer electrode spacing can improve MFC performance by lowering internal resistance, improving mass transport, and accelerating stabilization [46–48]. In this work, the DO_{MFC} electrodes were separated by a bacterial cellulose membrane, which had a high bio-affinity, water retention capacity, polymerization degree, and tensile strength and is also conducive to mass transport [15,49]. The compact structure of DO_{MFC} constrained the continuous thickening of the biofilm and reduced the internal resistance to mass transport. In addition, the biocompatibility and corrosion resistance of the anode material ensure the low internal resistance and stable performance of DO_{MFC} and reduce the risk of dramatic signal loss [50].

3.5. Operational traits of DO_{MFC} in batch mode

During the batch operation, the output voltage showed clear reproducible decline with DO decrease (Fig. 5A). The DO_{MFC} output voltage was stable within 0–5 min. The DO and the DO_{MFC} voltage decreased rapidly and steadily during the brief "saturation stage". Notably, the DO concentration and voltage were maintained at baseline levels (DO > 0.15 mg/L, V > 0.025 V) near the end of a cycle. Decerasing the cathode surface area from 30 to 20 cm^2 (Fig. 5B) als lead to a stable and reproducible signal of the DO_{MFC}. However, the peak voltage dropped from 0.607 to 0.464 V. The Al foam maintained its structural integrity under continuous operation, proving its rugged texture and excellent corrosion resistance (Fig. 5C).

During the "slow-fast-slow" decrease of the electrical signal, the initial brief stable or saturation stage indicated that the DO was saturated for the ORR (Lee and Do 2009). The ORR gradually slowed down because the H^+ concentration remained constant while the DO was consumed. After that, the DO depletion increased due to aerobic microorganisms' respiration (Fig. S7) and catalysis. At the end, the voltage and DO became relatively stable. Low DO concentrations lead to mass transfer losses and sluggish ORR kinetics [51], probably also due to the reduction of alternative electron acceptors (e.g., nitrate ions).

The selection of the optimal anode/cathode area ratio is a trade-off process. With the decrease in the anode/cathode area ratio, the anode potential will barely change, but the cathode potential will increase due to more reaction sites and less cathodic polarization, and the voltage will rise [52]. However, when the surface area of the cathode is equivalent to or greater than the anode, the electron generation by the anode limits the electricity output. In addition, the relatively large cathode surface area has a marginal effect on reducing cathode mass transfer loss and will increase the ohmic resistance of DO_{MFC} [53]. An anode/cathode ratio of 4/3 was selected in the following experiment setups.

3.6. Dynamic response of voltage to dissolved oxygen

The capability of DO_{MFC} was further investigated in continuous mode with different HRTs. With DO consumption by aerobic bacterial metabolism in the media and cathodic ORR, DO_{MFC} voltage decreased accordingly. Oxygen consumption at an HRT of 8 min was generally slower than at HRTs of 6.5 and 4.5 min. In addition, with the input of the aerated influent, the voltage signal bounced quickly (Fig. 6A-C). The maxima are 0.460 V and 0.387 V, respectively, for the HRT of 8 min, whereas they are 0.390 V and 0.307 V, respectively, for the HRT of 6.5 min. With HRT at 4.5 min, the voltage maxima were significantly attenuated, 0.273 V and 0.210 V, respectively. As the ORR reaction proceeded and aeration stopped, the DO concentration and voltage decreased rapidly and synchronously. The coefficients of determination (R^2) are 0.953, 0.964, and 0.989 for HRT of 8 mins, 6.5 mins, and 4.5 mins, respectively.

A higher flow rate (low HRT) may cause the loss of EABs in the anode, resulting in fewer electrons generation and lower voltage [54]. At the same time, high organic loading rates (OLRs) at high flow rates accelerated the growth of aerobic heterotrophic bacteria and oxygen consumption in the medium [55–57]. Although the power generation of DO_{MFC} and DO consumption fluctuated with HRT, DO concentration and voltage are highly positively correlated. The regression model with a short HRT had a higher R^2, i.e., it explained more variation. This may be attributed to increased flow rate, promoting solution mixing of the medium with the influent during aeration, lowering the peak voltage delay effect, and enhancing the correlation between DO and voltage.

The response characteristics of DO_{MFC} to DO were validated in

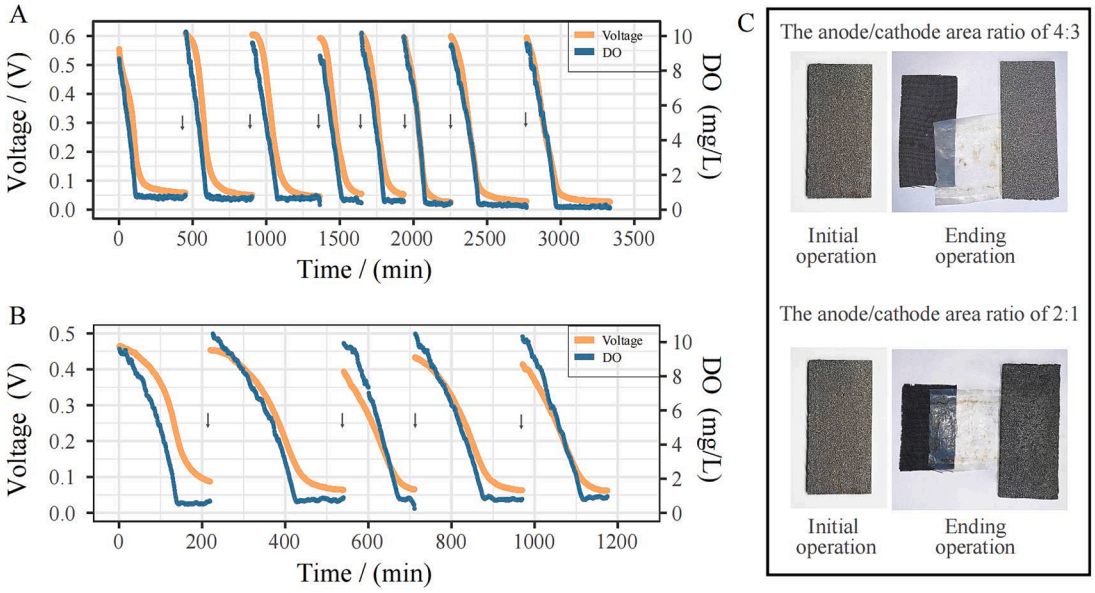

Fig. 5. Trend of output voltage of DOMFC and DO concentration in batch mode. (A) Operation of DOMFC with the anode/cathode area ratio of 4:3. (B) Operation of DOMFC with the anode/cathode area ratio of 2:1. (C) Integrity and breakage of anodes before and after operation of different DOMFC. Notes: the black arrow means the start of a new cycle.

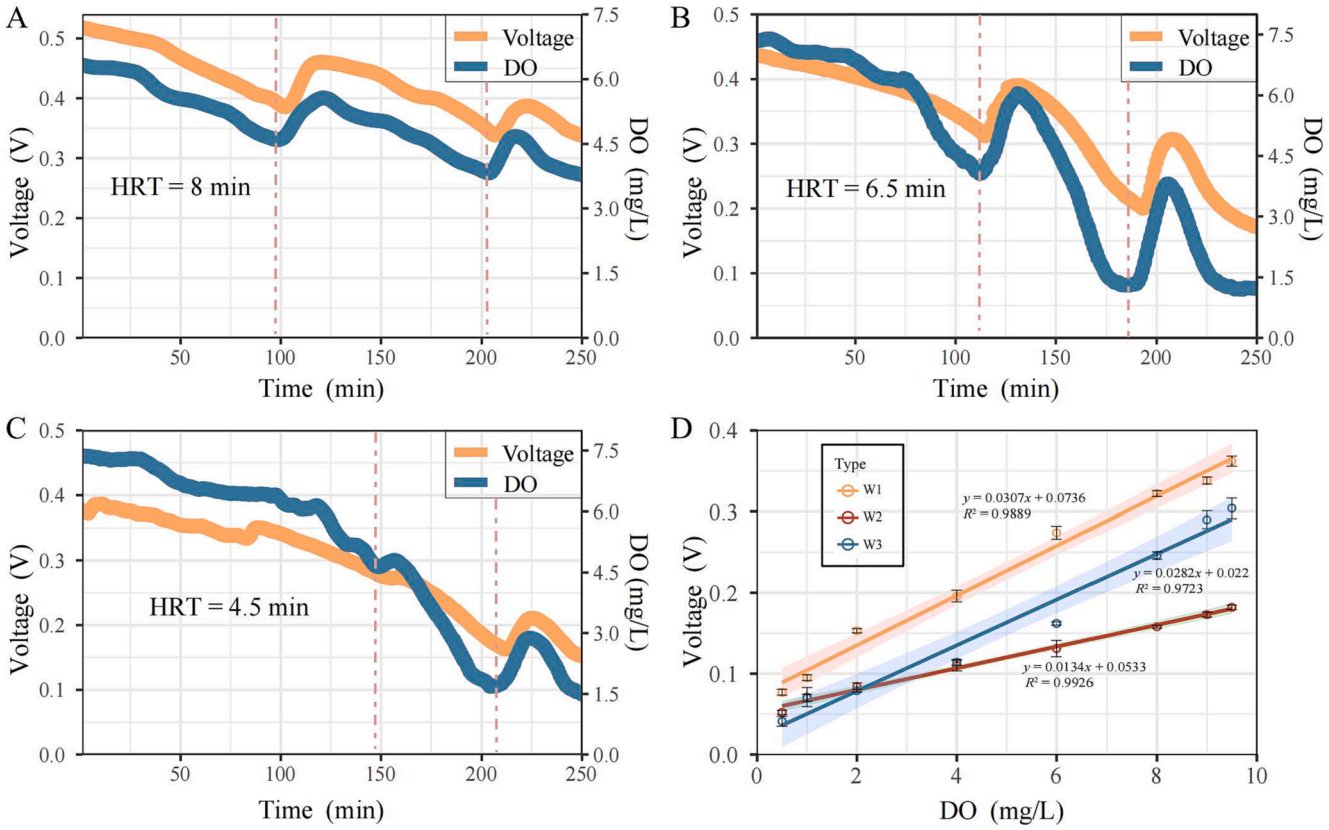

Fig. 6. The dynamic response characteristics of DOMFC to DO concentration. (A-C) Operation of DOMFC at different hydraulic retention times. The dotted line indicates partial substitution of the external solution. (D) Linear relationship between DO concentration and output voltage of DOMFC in different substrates. W1: glucose-based synthetic wastewater. W2: simulated polluted river water. W3: simulated fruit juice wastewater.

different wastewaters (i.e., glucose-based synthetic wastewater, simulated polluted river water, and simulated fruit juice wastewater) with significantly different COD concentrations. The results showed good linearity between voltage and DO concentration with R^2 of 0.9889, 0.9926, and 0.9723, respectively, thus confirming the broad range of DO_{MFC} applications (Fig. 6D). Significant differences in the maximum output voltage in different synthetic wastewaters may be related to the preference of nutrients by EAB [58]. DO_{MFC} had a specific and repeatable response to different DO, even if the solution COD concentration varied greatly. Fig. S8 presented the voltage output with COD degradation, which confirmed that DO_{MFC} is insensitive to COD changes and organic shock loadings. Both DO and ORR are the limiting factors for signal output.

3.7. Sensor compensation based on multi-data fusion strategy

The trends of DO_{MFC} voltage and DO concentration were highly convergent in all laboratory tests. As shown in Fig. 7A-B, a highly significant positive correlation between DO and DO_{MFC} voltage ($r = 0.976$, $p < 0.001$) was found for all the tested samples (three-tenths of the total sample size). Even so, the impact of water quality factors on electricity generation in DO_{MFC} will interfere with accurate DO monitoring, such as pH, conductivity, temperature, etc [12,13,59].

Since the pH in the batch experiments did not vary much, it was not used in the model construction of the dataset obtained from the reactor (Fig. S7). Conductivity is weakly negatively correlated with both DO ($r = -0.163$, $p < 0.001$) and DO_{MFC} voltage ($r = -0.245$, $p < 0.001$). Conductivity is usually positively correlated with salinity, so when it rises, it increases Henry's constant and reduces air solubility [60]. Elevated conductivity also can potentially affect cellular osmoregulation and metabolism [13]. A random forest (RF) algorithm was employed for importance ranking, and the results confirmed that DO concentration is the most critical factor impacting voltage output (Fig. 7C). As shown in Fig. 7D, the response rate of DO_{MFC} to DO is significantly higher than that to temperature. Temperature ranked second, with an increase in temperature enhancing mass transfer and thus decreasing the solubility of oxygen in water.

The calculation of the variance inflation factor (VIF) showed no serious multicollinearity between explanatory variables (Table S5). A multiple linear regression model incorporating all explanatory variables (except pH) and interaction effects had an adjusted R^2 of 0.994, explaining the dependent variable better than the model based on DO and voltage. Based on the multi-source data, the GA-BPNN model was constructed and optimized using the calibration of multi-source data fusion to the dependability and robustness of the biosensor. The performance parameters of GA-BPNN in laboratory experiments were depicted in Fig. 7E-F and Fig. S9C-D, with *RMSE*, *MAE* and R^2 of 0.0447, 0.0401, and 0.997, respectively, which gave more robust predictions compared to the linear regression model. In addition, the relative errors between predicted and observed data are concentrated in the range of 0–1%, and the two profiles represent the predicted and expected outputs, respectively, which also showed a high degree of overlap (Fig. 7E-F). After optimizing hyperparameters by GA, the number of convergence epochs for the best predictive model performance is only 28, preventing overfitting while training a neural network.

The predictive model was further tested in the field experiment. The pond water showed a DO of 1.5–6.2 mg/L, a conductivity of 0.286–0.366 ms/cm, a temperature of 15.88–19.5 °C, and a pH of 7.2–8.3. The DO_{MFC} gave maximum peak voltage of 0.143 V and 0.082 V under sunlight and shade conditions, respectively. DO concentrations and voltage level variations reveal a dynamic pattern of highly convergent trends (Fig. 7G). Photosysnthesis by water lilies and algae

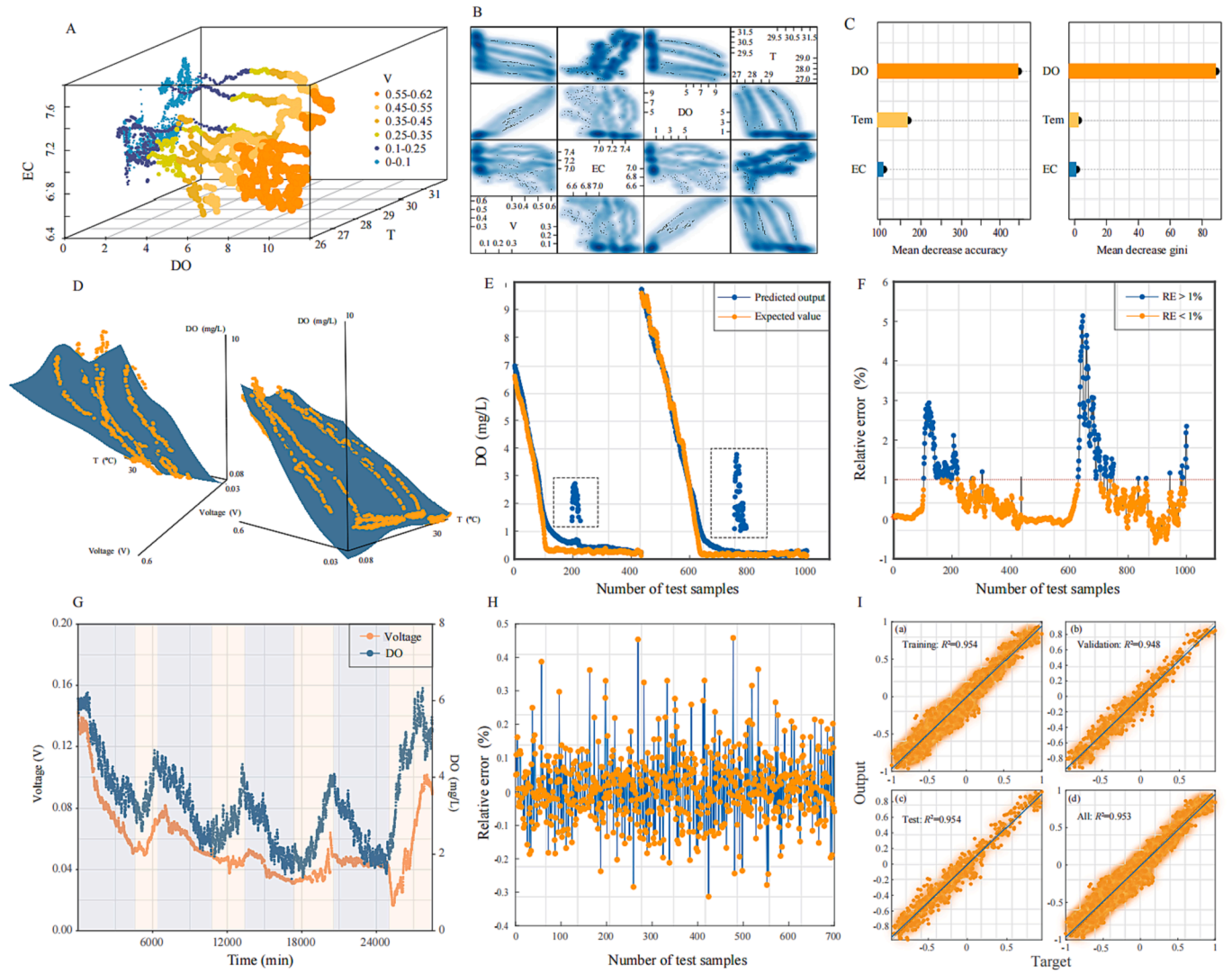

Fig. 7. Analysis of the experimental results in batch operation of DOMFC. (A) The three-dimensional image data of 3334 samples. Dividing voltage intervasl by different colors, thus showing the fourth-dimensional information. (B) Correlation between water quality factors. (C) Feature importance ranking of input factors. Mean decrease accuracy (MDA) indicates the magnitude of loss of accuracy by the model after excluding the variable. Mean decrease Gini (MDG) shows the effect of features on the node classification process. The value of mean decrease accuracy or mean decrease Gini score is proportional to the importance of that variable in the model. (D) Data visualization based on the multiple linear regression analysis involving two variables (voltage and water temperature). (E) The predicted results of GA-BPNN based on lab-scale tests. (F) Relative errors of GA-BPNN based on lab-scale results. (G) Variation of DO and DOMFC voltage under field conditions. The yellow and purple backgrounds indicate sunlight and non-sunlight (cloudy/rainy days and nighttime hours) conditions respectively. (H) Relative errors of GA-BPNN based on field results. (I) Fitting regression diagram of GA-BPNN model based on field results.

under sunlight produced oxygen, and the DO_{MFC} output voltage increased, while under prolonged shade conditions, the biological metabolic activities consumed DO substantially, and the voltage decreased. Notably, the conductivity of the pool water is only 1/20 of that of the culture medium, and the monitoring environment contains inherent heavy metal risks. The relative errors between the GA-BPNN model outputs and measured values are within 0.5%, indicating that the prediction system is noise-resistant and robust (Fig. 7H). During a 20-day operating period, DO_{MFC} still showed high predictive performance with an R^2 of 0.954 (Fig. 7I). Mean Absolute Error (*MAE*) is a measure of the difference between predicted and measured values with noise robustness to reflect the operation of sensors in complex environments objectively, which was only 0.1620, indicating DO_{MFC} can feed reliable monitoring data to decision-makers.

The DO concentration and the output voltage of the DO_{MFC} showed perfect linearity, which gives the DO_{MFC} the potential to be an independent monitoring unit. By introducing additional influencing factors to create the GA-BPNN, this model can be coupled with current water quality monitoring systems to achieve more accurate DO prediction (Table 1). Our experimental results showed that the GA-BPNN effectively mapped DO concentration and input factors such as voltage. Compared to mechanical and numerical models, the GA-BP model does not require sophisticated mathematical models or calibration parameters and can compensate for significant external disturbances.

4. Conclusions and future perspectives

The current study presents a high-accuracy real-time DO biosensor based on iMFC at low cost, which performed excellently in monitoring natural and artificial waters. A prediction model based on multiple environmental indexes using a multi-source data fusion strategy further improved its performance. Besides, necessary and inexpensive water quality sensors can be used for DO_{MFC} sensor compensation. The portable and affordable low-power sensor technology system

Table 1
Performance comparison of various MFC-based DO biosensors.

Device types	Signal	Real-time monitoring capability	Response time (min)	Sensitivity	Measurement range (mg/L)	Experimental Scenario	Model Evaluation Metrics	Reference
Single-chamber MFC	Current density	Incapable	≤4	Not mentioned	≤8.8 ± 0.3	Laboratory	$R^2 = 0.9912$	[11]
Sediment MFC	Voltage	Incapable	Not mentioned	0.83–1.96 mV (mg L^{-1})$^{-1}$ cm^{-2}	0–9	Laboratory Bay	$R^2 = 0.9576$ $R^2 = 0.8897$	[12]
Single-chamber MFC	Voltage	Incapable	3.3	1.11 ± 0.47 mV (mg L^{-1})$^{-1}$ cm^{-2}	0.2–4.6 3.9–9.6 0–6.44	Laboratory	*RMSE* = 0.7 *RMSE* = 1 *RMSE* = 0.6	[13]
Single-chamber MFC	Current density	Incapable	≤30	Not mentioned	0–8	Laboratory	$R^2 = 0.71$ *RE* (6.25%-15.15%)	[61]
Free-chamber (DO_{MFC})	Voltage	capable	≤1	2.15 mV (mg L^{-1})$^{-1}$ cm^{-2}	0.15–9.5	Laboratory Pond	$R^2 = 0.997$ $R^2 = 0.924$	This study

demonstrated here holds promise for the long-term, *in-situ* monitoring of DO (Table S6). Given the possibility of sudden environmental shocks (water level anomalies, mechanical disturbances, non-EABs invasion, etc.), further research will evaluate the long-term stability of DO_{MFC} under extreme environmental conditions.

With a price of USD 13.74, a single DO_{MFC} sensor is an order of magnitide cheaper than competing technologies (Table S7-8). Moreover, up to 10 DO_{MFC}s can be integrated into a Raspberry Pi-based data acquisition and compensation platform, which creates a favorable application in various watersheds, cross-sections, and depths of natural or artificial waterbodies (e.g., rivers, lakes, reservoirs, and wastewater treatment plants) (Fig. S11). The DO_{MFC} can quickly obtain three-dimensional, high-precision DO information and draw a three-dimensional distribution heatmap by fusing IoT, big data, and data visualization technology. This information can be widely used for water quality evaluation, aeration guidance, and remediation supervision. Beyond this, DO_{MFC} also be used to evaluate pollutants toxicity, COD level, and other indexes, which creates a promosing functional improvement possibility of the biosensor raised in the current work.

Declaration of Competing Interest

The authors declare that they have no known competing financial interests or personal relationships that could have appeared to influence the work reported in this paper.

Data availability

Data will be made available on request.

Acknowledgments

This study was financially supported by the Key Research and Development Program of Sichuan Province (2021YJ0495), Fundamental Research Funds for the Central Universities (20826041D4303, 20826041E4314, 2682021CX084), Startup Funding of the Chinese Academy of Sciences (2017-020), National Key Research and Development Project of China (2018YFC1802601), Strategic Priority Research Program of Chinese Academy of Sciences (XDB40020300), National Natural Science Foundation of China (41877400, 42007294), State Key Laboratory of Environmental Geochemistry (SKLEG2018911), State Key Laboratory of Microbial Technology Foundation (M2017-01), National Ocean 13th Five-Year Plan (The exploration of Indian Ocean polymetallic sulfide resources), and German Research Foundation (SFB 1253/1 2017 and HA 5453/14-1).

Appendix A. Supplementary data

Supplementary data to this article can be found online at https://doi.org/10.1016/j.cej.2023.146064.

References

[1] L. Zhu, W. Shi, B. Van Dam, L. Kong, J. Yu, B. Qin, Algal accumulation decreases sediment nitrogen removal by uncoupling nitrification-denitrification in shallow eutrophic lakes, Environ. Sci. Tech. 54 (10) (2020) 6194–6201.
[2] X. Zhao, X. Ma, B. Chen, Y. Shang, M. Song, Challenges toward carbon neutrality in China: Strategies and countermeasures, Resour. Conserv. Recycl. 176 (2022) 105959.
[3] J.-Y. Lu, X.-M. Wang, H.-Q. Liu, H.-Q. Yu, W.-W. Li, Optimizing operation of municipal wastewater treatment plants in China: the remaining barriers and future implications, Environ. Int. 129 (2019) 273–278.
[4] L. Luo, M. Dzakpasu, B. Yang, W. Zhang, Y. Yang, X.C. Wang, A novel index of total oxygen demand for the comprehensive evaluation of energy consumption for urban wastewater treatment, Appl. Energy 236 (2019) 253–261.
[5] H. Wang, D. Chen, Y. Chen, J. Liu, J. Xu, A. Zhu, F. Long, Development of novel handheld optical fiber dissolved oxygen sensor and its applications, Anal. Chim. Acta 1200 (2022), 339587.
[6] H.V. Hamelers, A. Ter Heijne, T.H. Sleutels, A.W. Jeremiasse, D.P. Strik, C. J. Buisman, New applications and performance of bioelectrochemical systems, Appl. Microbiol. Biotechnol. 85 (6) (2010) 1673–1685.
[7] B.E. Logan, B. Hamelers, R. Rozendal, U. Schröder, J. Keller, S. Freguia, P. Aelterman, W. Verstraete, K. Rabaey, Microbial fuel cells: methodology and technology, Environ. Sci. Tech. 40 (17) (2006) 5181–5192.
[8] F. Guo, Y. Liu, H. Liu, Hibernations of electroactive bacteria provide insights into the flexible and robust BOD detection using microbial fuel cell-based biosensors, Sci. Total Environ. 753 (2021), 142244.
[9] R. Lu, Y.H. Chen, J.M. Wu, D.S. Chen, Z.B. Wu, E.R. Xiao, *In situ* COD monitoring with use of a hybrid of constructed wetland-microbial fuel cell, Water Res. 210 (2022), 117957.
[10] Z. Lin, S. Cheng, Y. Sun, H. Li, B. Jin, Realizing BOD detection of real wastewater by considering the bioelectrochemical degradability of organic pollutants in a bioelectrochemical system, Chem. Eng. J. 444 (2022), 136520.
[11] Y.F. Zhang, I. Angelidaki, A simple and rapid method for monitoring dissolved oxygen in water with a submersible microbial fuel cell (SBMFC), Biosens. Bioelectron. 38 (1) (2012) 189–194, https://doi.org/10.1016/j.bios.2012.05.032.
[12] N. Song, Z.S. Yan, H.C. Xu, Z.B. Yao, C.H. Wang, M. Chen, Z.W. Zhao, Z.L. Peng, C. L. Wang, H.L. Jiang, Development of a sediment microbial fuel cell-based biosensor for simultaneous online monitoring of dissolved oxygen concentrations along various depths in lake water, Sci. Total Environ. 673 (2019) 272–280.
[13] L.G. Olias, A.R. Otero, P.J. Cameron, M. Di Lorenzo, A soil microbial fuel cell-based biosensor for dissolved oxygen monitoring in water, Electrochim. Acta 362 (2020) 137108.
[14] S.E. Ellis, S. Gupta, F.N. Ashar, J.S. Bader, A.B. West, D.E. Arking, RNA-Seq optimization with eQTL gold standards, BMC Genomics 14 (1) (2013) 1–11.
[15] P. Chen, T. Zhang, Y. Chen, H. Ma, Y.u. Wang, W. Liu, Y. Wang, G. Zhou, R. Qing, Y. Zhao, H. Xu, L. Hao, C. Wang, F. Xu, Integrated chamber-free microbial fuel cell for wastewater purification and bioenergy generation, Chem. Eng. J. 442 (2022) 136091.
[16] M. Sajjad, M. Nasir, K. Muhammad, S. Khan, Z. Jan, A.K. Sangaiah, M. Elhoseny, S. W. Baik, Raspberry Pi assisted face recognition framework for enhanced law-enforcement services in smart cities, Futur. Gener. Comput. Syst. 108 (2020) 995–1007.
[17] R. Wang, H.-Y. Bi, A predictive model for chinese children with developmental dyslexia—Based on a genetic algorithm optimized back-propagation neural network, Expert Syst. Appl. 187 (2022), 115949.

[18] J. Ma, J.Y. Tang, S. Wang, Z.L. Chen, X.D. Li, Y.H. Li, Illumina sequencing of bacterial 16S rDNA and 16S rRNA reveals seasonal and species-specific variation in bacterial communities in four moss species, Appl. Microbiol. Biotechnol. 101 (17) (2017) 6739–6753.
[19] P. Choudhury, R.N. Ray, T.K. Bandyopadhyay, B. Basak, M. Muthuraj, B. Bhunia, Process engineering for stable power recovery from dairy wastewater using microbial fuel cell, Int. J. Hydrogen Energy 46 (4) (2021) 3171–3182.
[20] Z. He, Development of microbial fuel cells needs to go beyond "power density", ACS Energy Lett. 2 (3) (2017) 700–702.
[21] S. Jung, J.M. Regan, Influence of external resistance on electrogenesis, methanogenesis, and anode prokaryotic communities in microbial fuel cells, Appl. Environ. Microbiol. 77 (2) (2011) 564–571.
[22] R. Kumar, L. Singh, A.W. Zularisam, Exoelectrogens: recent advances in molecular drivers involved in extracellular electron transfer and strategies used to improve it for microbial fuel cell applications, Renew. Sust. Energ. Rev. 56 (2016) 1322–1336.
[23] P.S. Bonanni, G.D. Schrott, L. Robuschi, J.P. Busalmen, Charge accumulation and electron transfer kinetics in Geobacter sulfurreducens biofilms, Energ. Environ. Sci. 5 (3) (2012) 6188–6195.
[24] Y. Zhang, Q. Xu, G. Huang, L. Zhang, Y. Liu, Effect of dissolved oxygen concentration on nitrogen removal and electricity generation in self pH-buffer microbial fuel cell, Int. J. Hydrogen Energy 45 (58) (2020) 34099–34109.
[25] M. Kobayashi, R. Agari, Y. Kigo, A. Terada, Efficient oxygen supply and rapid biofilm formation by a new composite polystyrene elastomer membrane for use in a membrane-aerated biofilm reactor, Biochem. Eng. J. 183 (2022), 108442.
[26] W. Lin, M.V. Coppi, D. Lovley, Geobacter sulfurreducens can grow with oxygen as a terminal electron acceptor, Appl. Environ. Microbiol. 70 (4) (2004) 2525–2528.
[27] A. Prévoteau, P. Clauwaert, F.-M. Kerckhof, K. Rabaey, Oxygen-reducing microbial cathodes monitoring toxic shocks in tap water, Biosens. Bioelectron. 132 (2019) 115–121.
[28] K. Rabaey, N. Boon, M. Hofte, W. Verstraete, Microbial phenazine production enhances electron transfer in biofuel cells, Environ. Sci. Tech. 39 (9) (2005) 3401–3408.
[29] M.A. TerAvest, M.A. Rosenbaum, N.J. Kotloski, J.A. Gralnick, L.T. Angenent, Oxygen allows *Shewanella oneidensis* MR-1 to overcome mediator washout in a continuously fed bioelectrochemical system, Biotechnol. Bioeng. 111 (4) (2014) 692–699.
[30] J.W. Yang, S.A. Cheng, P. Li, H.B. Huang, K.F. Cen, Sensitivity to Oxygen in Microbial Electrochemical Systems Biofilms, Iscience 13 (2019) 163-+.
[31] Y. Wang, H. Zheng, Y. Chen, Q. Wen, J. Wu, Macroporous composite capacitive bioanode applied in microbial fuel cells, Chin. Chem. Lett. 31 (1) (2020) 205–209.
[32] H. Wu, H. Tan, L. Chen, B. Yang, Y. Hou, L. Lei, Z. Li, Stainless steel cloth modified by carbon nanoparticles of Chinese ink as scalable and high-performance anode in microbial fuel cell, Chin. Chem. Lett. 32 (8) (2021) 2499–2502.
[33] H. Xu, D. Wang, P. Yang, A. Liu, R. Li, L. Xiao, J. Zhang, Z. Qu, M. An, FeS encapsulated hierarchical porous S, N-dual-doped carbon for oxygen reduction reaction facilitation in Zn–air batteries, Sustainable Energy Fuels 5 (10) (2021) 2695–2703.
[34] Y. Liao, Y. Wang, J. Liu, Y. Tang, C. Wu, Y. Chen, Ordered Mesoporous Carbon Confined Highly Dispersed PtCo Alloy for the Oxygen Reduction Reaction: The Effect of Structure and Composition on Performance, Ind. Eng. Chem. Res. 60 (41) (2021) 14728–14736.
[35] M. Mutschlechner, N. Praeg, P. Illmer, Soil-Derived Inocula Enhance Methane Production and Counteract Common Process Failures During Anaerobic Digestion, Front. Microbiol. 11 (2020), 572759.
[36] R. López-Mondéjar, C. Algora, P. Baldrian, Lignocellulolytic systems of soil bacteria: a vast and diverse toolbox for biotechnological conversion processes, Biotechnol. Adv. 37 (6) (2019), 107374.
[37] Z. Gong, H. Yu, J. Zhang, F. Li, H. Song, Microbial electro-fermentation for synthesis of chemicals and biofuels driven by bi-directional extracellular electron transfer, Synth. Syst. Biotechnol. 5 (4) (2020) 304–313.
[38] W. Khawdas, K. Watanabe, H. Karatani, Y. Aso, T. Tanaka, H. Ohara, Direct electron transfer of Cellulomonas fimi and microbial fuel cells fueled by cellulose, J. Biosci. Bioeng. 128 (5) (2019) 593–598.
[39] Y. Yang, Z. Wang, C. Gan, L.H. Klausen, R. Bonné, G. Kong, D. Luo, M. Meert, C. Zhu, G. Sun, J. Guo, Y. Ma, J.T. Bjerg, J. Manca, M. Xu, L.P. Nielsen, M. Dong, Long-distance electron transfer in a filamentous Gram-positive bacterium, Nat. Commun. 12 (1) (2021).
[40] Z. Xu, C. Qi, L. Zhang, Y. Ma, J. Li, G. Li, W. Luo, Bacterial dynamics and functions for gaseous emissions and humification in response to aeration intensities during kitchen waste composting, Bioresour. Technol. 337 (2021), 125369.
[41] J. Visvalingam, H. Wang, T.C. Ells, X. Yang, Facultative anaerobes shape multispecies biofilms composed of meat processing surface bacteria and Escherichia coli O157: H7 or Salmonella enterica serovar Typhimurium, Appl. Environ. Microbiol. 85 (17) (2019) e01123–e10219.
[42] A. Venkataraman, M. Rosenbaum, J.B. Arends, R. Halitschke, L.T. Angenent, Quorum sensing regulates electric current generation of Pseudomonas aeruginosa PA14 in bioelectrochemical systems, Electrochem. Commun. 12 (3) (2010) 459–462.
[43] G.G. Halfeld, E.J.R. de Almeida, V. Reginatto, A.R. de Andrade, Acclimatization of a microbial consortium into a stable biofilm to produce energy and 1, 3-propanediol from glycerol in a microbial fuel cell, Int. J. Hydrogen Energy 47 (49) (2022) 21241–21252.
[44] J. Gao, N. Shi, X. Guo, Y. Li, X. Bi, Y. Qi, J. Guan, B. Jiang, Electrochemically selective ammonia extraction from nitrate by coupling electron-and phase-transfer reactions at a three-phase interface, Environ. Sci. Tech. 55 (15) (2021) 10684–10694.
[45] A. Ter Heijne, O. Schaetzle, S. Gimenez, F. Fabregat-Santiago, J. Bisquert, D. P. Strik, F. Barriere, C.J. Buisman, H.V. Hamelers, Identifying charge and mass transfer resistances of an oxygen reducing biocathode, Energ. Environ. Sci. 4 (12) (2011) 5035–5043.
[46] M.I. Simeon, R. Freitag, Influence of electrode spacing and fed-batch operation on the maximum performance trend of a soil microbial fuel cell, Int. J. Hydrogen Energy 47 (24) (2022) 12304–12316.
[47] R. Rossi, B.E. Logan, Impact of reactor configuration on pilot-scale microbial fuel cell performance, Water Res. 225 (2022) 119179.
[48] D.A. Jadhav, A.A. Carmona-Martínez, A.D. Chendake, S. Pandit, D. Pant, Modeling and optimization strategies towards performance enhancement of microbial fuel cells, Bioresour. Technol. 320 (2021), 124256.
[49] S.U. Islam, M. Ul-Islam, H. Ahsan, M.B. Ahmed, A. Shehzad, A. Fatima, J.K. Sonn, Y.S. Lee, Potential applications of bacterial cellulose and its composites for cancer treatment, Int. J. Biol. Macromol. 168 (2021) 301–309.
[50] P. Bombelli, A. Savanth, A. Scarampi, S.J.L. Rowden, D.H. Green, A. Erbe, E. Årstøl, I. Jevremovic, M.F. Hohmann-Marriott, S.P. Trasatti, E. Ozer, C.J. Howe, Powering a microprocessor by photosynthesis, Energ. Environ. Sci. 15 (6) (2022) 2529–2536.
[51] M. Kumar, T.C. Nagaiah, Tuning the interfacial chemistry for stable and high energy density aqueous sodium-ion/sulfur batteries, J. Mater. Chem. A 10 (24) (2022) 12984–12996.
[52] S. Cheng, B.E. Logan, Increasing power generation for scaling up single-chamber air cathode microbial fuel cells, Bioresour. Technol. 102 (6) (2011) 4468–4473.
[53] S. Liu, F. Lu, D. Qiu, X. Feng, Wetland plants selection and electrode optimization for constructed wetland-microbial fuel cell treatment of Cr (VI)-containing wastewater, J. Water Process Eng. 49 (2022), 103040.
[54] Y. Ye, H.H. Ngo, W. Guo, S.W. Chang, D.D. Nguyen, X. Zhang, S. Zhang, G. Luo, Y. Liu, Impacts of hydraulic retention time on a continuous flow mode dual-chamber microbial fuel cell for recovering nutrients from municipal wastewater, Sci. Total Environ. 734 (2020), 139220.
[55] Z. Zhang, J. Qiu, R. Xiang, H. Yu, X. Xu, L. Zhu, Organic loading rate (OLR) regulation for enhancement of aerobic sludge granulation: Role of key microorganism and their function, Sci. Total Environ. 653 (2019) 630–637.
[56] Y.-M. Zheng, H.-Q. Yu, S.-J. Liu, X.-Z. Liu, Formation and instability of aerobic granules under high organic loading conditions, Chemosphere 63 (10) (2006) 1791–1800.
[57] D.M. Kennes-Veiga, L. Gonzalez-Gil, M. Carballa, J.M. Lema, The organic loading rate affects organic micropollutants' cometabolic biotransformation kinetics under heterotrophic conditions in activated sludge, Water Res. 189 (2021), 116587.
[58] F. Rezaei, D. Xing, R. Wagner, J.M. Regan, T.L. Richard, B.E. Logan, Simultaneous cellulose degradation and electricity production by Enterobacter cloacae in a microbial fuel cell, Appl. Environ. Microbiol. 75 (11) (2009) 3673–3678.
[59] T. Ouyang, X. Hu, X. Shi, W. Liu, J. Lu, W. Li, Mathematical modeling and performance evaluation of a cathodic bi-population microfluidic microbial fuel cell, Energ. Conver. Manage. 267 (2022), 115900.
[60] J. Haarhoff, J.K. Edzwald, Adapting dissolved air flotation for the clarification of seawater, Desalination 311 (2013) 90–94.
[61] M. Christwardana, L.A. Yoshi, I. Setyonadi, M.R. Maulana, A. Fudholi, A novel application of simple submersible yeast-based microbial fuel cells as dissolved oxygen sensors in environmental waters, Enzyme Microb. Technol. 149 (2021).